batteries

MDPI

Article

Revealing Lithiation Kinetics and Battery Degradation Pathway in $LiMn_2O_4$-Based Commercial Cathodes via Electrochemical Strain Microscopy

Denis Alikin *, Boris Slautin and Andrei Kholkin

School of Natural Sciences and Mathematics, Ural Federal University, 620000 Ekaterinburg, Russia
* Correspondence: denis.alikin@urfu.ru; Tel.: +343-261-74-36

Abstract: The capacity fade during the cycling of lithium batteries is a key factor limiting further progress in the improvement of electric vehicles, wearable electronic devices, alternative energy sources, etc. One of the main reasons for capacity loss is battery cathode degradation, which significantly influences the battery lifetime. Despite in-depth knowledge of battery degradation at the chemical level, the kinetics of the degradation at the resolution of the individual elements of the cathode are not fully understood. Here, we studied lithiation kinetics in commercial cathodes based on lithium manganese spinel using the electrochemical strain microscopy local method. Supported by the experimental finding, the "viscous fingers" model of lithium ions intercalation–deintercalation in individual particles of the cathode was proposed. The non-linear dynamics of the lithiation front were suggested to be stimulated by the non-uniform stress field and gradient of the chemical potential. Irregularity of the lithiation front causes the formation of the residual lithiated pocket in the delithiated particles, which effectively reduces the volume available for chemical reaction. The obtained results shed further light on the degradation of the lithium battery cathodes and can be applicable for other cathode materials.

Keywords: intercalation kinetics; viscous fingers; lithiation reaction; nanoscale resolution

Citation: Alikin, D.; Slautin, B.; Kholkin, A. Revealing Lithiation Kinetics and Battery Degradation Pathway in $LiMn_2O_4$-Based Commercial Cathodes via Electrochemical Strain Microscopy. *Batteries* **2022**, *8*, 220. https://doi.org/10.3390/batteries8110220

Academic Editor: Carlos Ziebert

Received: 24 September 2022
Accepted: 2 November 2022
Published: 5 November 2022

1. Introduction

Lithium manganese spinel ($Li_xMn_2O_4$, LMO) is an attractive cathode material for rechargeable Li-ion batteries because of its low cost, weak environmental impact, relatively high discharge potential of ~4 V, and capacity of about 148 mA h g^{-1} [1,2]. At the same time, apparent capacity fade during cycling, especially at elevated temperatures (>50 °C), significantly limits applications of LMO [3]. Despite the long history of LMO and in-depth studies by electrochemical methods, the concrete mechanism of the LMO cathode degradation is still not clear [4–6]. The generally accepted mechanism of degradation is manganese dissolution into the electrolyte, which mostly occurs during the first several cycles [3,7,8]. Manganese dissolution originates from the disproportional reaction $2Mn^{3+} \rightarrow Mn^{+2} + Mn^{4+}$, which leads to the formation of $Mn^{4+}(O^{2-})_2$ oxide near the surface of the particles and dissolving Mn^{2+} ions in the electrolyte [9]. Another discussed pathway of degradation is through the phase transitions $2\ LiMn_2O_4 \rightarrow MnO + Li_2Mn_3O_7$ and $4\ LiMn_2O_4 \rightarrow Mn_3O_4 + Li_4Mn_5O_{12}$ with the dissolution of MnO and Mn_3O_4 [3,10]. An appearance of Mn_3O_4 near the surface of particles, as a result of delithiation during the first several cycles and its continuous disappearance, was observed recently by Raman spectroscopy and scanning transmission electron microscopy (STEM) [11,12]. Manganese dissolution was reported to significantly depend on the "state of charge" of cathodes and to accelerate with delithiation due to the growth of discharge potential [13].

Another important issue of the material is a sequence of phase transitions occurring during lithiation/delithiation cycles. In a fully lithiated state, LMO has *Fd*3*m* structure [14,15]: lithium ions occupy the tetrahedral 8a position, Mn^{3+} and Mn^{+4} ions are

randomly placed in octahedral 16d crystallographic positions with a 1:1 ratio, and oxygen ions occupy 32e sites. Lithium extraction is associated with the change in oxidation state from Mn^{3+} to Mn^{4+}. The crystalline structure of LMO transforms to $F\bar{4}3m$ space group of symmetry during delithiation towards $Li_{0.5}Mn_2O_4$ composition [2]. A fully delithiated λ-MnO_2 has a structure similar to a $LiMn_2O_4$ cubic structure, but with empty 8e lithium positions [14]. $Fd3m \rightarrow F\bar{4}3m$ transition during the lithiation/delithiation cycle is commonly associated with the volumetric change, responsible for the stress accommodation and particle crackling [16].

The structure of LMO admits over-lithiation to the $Li_2Mn_2O_4$ state under discharge potential of around 3 V [2], which is associated with the structural transition to $I4_1/amd$ tetragonal spinel, accompanied by the transformation of isotropic $Mn^{4+}O_6$ octahedra to distorted $Mn^{3+}O_6$ with anisotropic volume change around ~16% (Jan–Teller distortion) and the appearance of the local mechanical strain [3,17,18]. STEM visualization of the $Li_2Mn_2O_4$ tetragonal phase reveals the formation of the twinned structure compensating the stress relief and hampering lithium diffusion [6]. Jan–Teller distortion also leads to particle cracking [4,19]. In commercial cathodes, the degree of lithiation is usually limited to a range of x from 0.6 to 1 to exclude Jan–Teller distortions. However, the appearance of the tetragonal phase at the surface of the particles has been reported even without the over-lithiation of the cathode [18]. Researchers have proposed that this Mn^{+3}-rich $Li_2Mn_2O_4$ layer can also impact on capacity fade by accelerating of Mn dissolution through the disproportional reaction, presumably due to the overpotential in local areas of the particles [18].

The local measurements of the Li ions' diffusion pathways in electrode materials are rarely reported and mainly utilize high-resolution transmission electron microscopy imaging [11,20–22]. The heterogeneity of the transport is noticed for micro-scale particles of different compositions [6,16,20,23–28]. In crystalline $LiFePO_4$ (LFP), the delithiation reaction proceeds at many points of the crystal surface and is significantly determined by the kinetics of dislocations and stress field distribution [20]. In LMO, the heterogeneity was connected to local overpotentials revealed even under uniform electrical load [23]. Electrochemical experiments in LMO demonstrated the principal role of particle size: nanoparticles smaller than 15 nm show lithiation without the formation of the spatially separated lithiated areas [22]. Operando liquid X-ray microscopy reveals intercalation to be significantly dependent on the particle's shape: ellipsoidal particles intercalate sequentially, whereas platelet particles intercalate concurrently, which is controlled by the local current density [29]. In $LiNi_{o.6}Co_{0.2}Mn_{0.2}O_2$ particles, the heterogeneity of Li-ion distribution and capacity fade were explained by the imperfect electrical contact between the cathode and electrolyte, leading to the increase in shear stress at the particle interface [26]. In LFP-based commercial cathodes, delithiation was also shown to start from several regions on the surface of the particles and nonuniformly propagate into the bulk, which was attributed to the inhomogeneity of the electrical contacts and stress field distribution [30]. A recent report on LFP commercial cathodes with nanosized particles revealed the importance of the local environment [24]. The nanoscale particles inside aggregates were shown to experience more pronounced reaction heterogeneity than the nanoparticles dispersed in the electrolyte [24].

Despite these efforts, the understanding of lithiation dynamics at the scale of individual grains is still elusive. The electrochemical strain microscopy (ESM) method gives a unique opportunity to study lithium distribution with high spatial resolution [31–33] without the need for surface irradiation by high-energy electron or X-ray beams. ESM signal in a low-frequency regime is directly connected to the Vegard expansion of the lattice [32,34]. The solid basis for the quantification of the low-frequency ESM method [34,35] was suggested, which allows evaluation of the lithium-ion concentration and diffusion coefficients [32,34,35].

Our previous studies were mostly focused on the development of ESM methodology rather than on its application to specific materials [34,35]. The current work fills this gap

and concentrates mainly on the material chemistry and the kinetics of battery degradation. The change in the lithium ions' distribution under cathode cycling was studied, and local insight into the cathode degradation is given. The model of lithium ions' intercalation/deintercalation was proposed for LMO-based cathodes, which indicates their vulnerability. The performed research is important for further modification of battery production and the improvement of lithium battery-based technology for energy storage.

2. Materials and Methods

Commercial cathodes from Li-ion batteries were produced by Robert BOSCH Gmbh. The batteries were cycled in cylindrical cells. Cathodes with a 100% "state of health" (SOH) were subjected to 3 charge/discharge cycles with a 1 C rate (fresh). Cathodes with 80% SOH (aged) were cycled 106 times with a 1 C charge rate and a 16 C discharge rate and then 3 more times with a 1 C rate of charge and discharge, leading to capacity fade (Figure 1). Cathodes with a 100% "state of charge" (SOC) have a $Li_{0.6}Mn_2O_4$ state, while cathodes with 0% SOC have a $Li_{0.9}Mn_2O_4$ state (Table 1). After cycling, the batteries were opened in the glovebox, the cathodes were extracted, and the electrolyte was washed out using dimethyl carbonate. After drying, the cathodes were embedded in epoxy resin and polished mechanically with step-by-step decreasing abrasive. At the final stage, fine argon ion beam milling was performed. Detailed information about the properties of the cathodes and the sample preparation procedure can be found elsewhere [36].

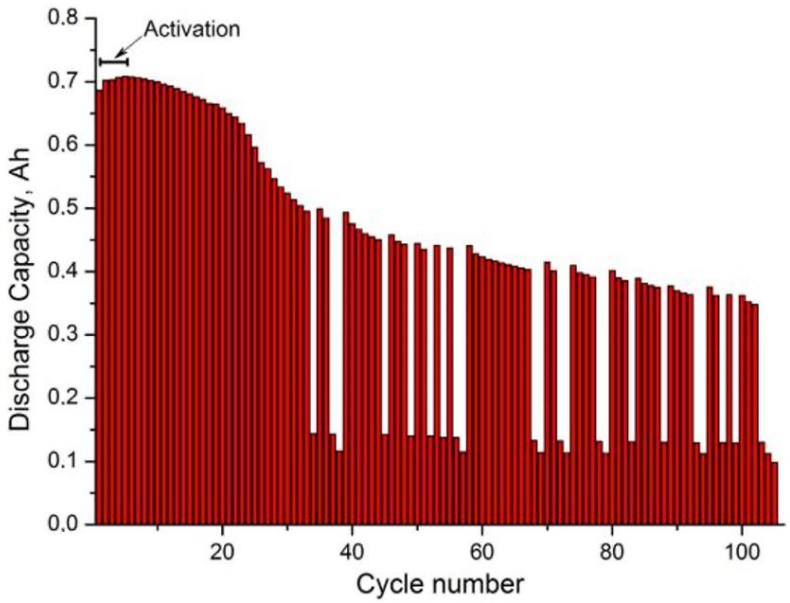

Figure 1. Discharge capacity versus cycle number of the aged cell. The first 5 cycles present a capacity increase due to activation of the cell. The very low capacity is due to a failure with the cycling instrument. Reprinted from *Journal of Power Sources*, Vol. 268, Luchkin, S.Y.; Amanieu, H.Y.; Rosato, D.; Kholkin, A.L., Li Distribution in Graphite Anodes: A Kelvin Probe Force Microscopy Approach, Page No. 889, Copyright (2014), with permission from Elsevier.

Table 1. The parameters of the LMO-based cathodes.

Sample	SOC, %	SOH, %	Lattice Parameter, Å	Li-ion Concentration, m^{-3}
$Li_{0.94}Mn_2O_4$	0	100	8.18	21.4×10^{25}
$Li_{0.61}Mn_2O_4$	100	100	8.09	14.4×10^{25}
$Li_{0.89}Mn_2O_4$	0	80	8.18	20.3×10^{25}
$Li_{0.65}Mn_2O_4$	100	80	8.11	15.2×10^{25}

Electrochemical strain microscopy (ESM) measurements were performed in low-frequency mode, where Vegard expansion of the surface under modulated low-frequency voltage is proportional to the local concentration of the lithium ions. It should be noted that the low-frequency ESM mechanism is principally different from the high-frequency ESM, where the signal is originated fromthe local variation in the dielectric properties [28]. The ESM signal is, in part, influenced by the topography [35], which seems to be unavoidable, because the topography of the cathodes correlates with the concurrent electrochemical process [37,38]. Because of that, the flattest particles in the cathodes were inspected in the measurements. The measurements were performed at the MFP-3D-SA scanning probe microscope (Oxford Instruments, Abingdon, U.K.) in a dry nitrogen atmosphere. Scansens HA_NC_W_2C (Bremen, Germany) silicon probes with conductive carbide wolfram coating were used. The parameters of the probe were chosen to achieve a minimum value of the low-frequency shape factor, which maximizes the amplification of the weak electromechanical signal [35,39]. Voltage with 5 V_{p-p} amplitude and 3.5 kHz frequency was applied to the probe. The details of the low-frequency ESM approach, including experimental realization and calculation of the lithium concentrations, are given in Refs. [32,35]. As the top part of the particle was removed by polishing, the ESM signal captured on the surface was interpreted as a 2D section of the active particle, allowing us to extract information about the distribution of the lithium ion concentration inside the particle bulk.

3. Results

We start with ESM characterization of the lithium concentration in four studied cathodes. ESM revealed the non-uniform distribution of lithium concentration in the volume of the particle for all studied cathodes (Figure 2). The distribution of the lithium ions was in part correlated with the position of the cracks (Figure 2), which, however, can be caused by the mechanical strain appearing during the lattice transformation in the process of battery cycling.

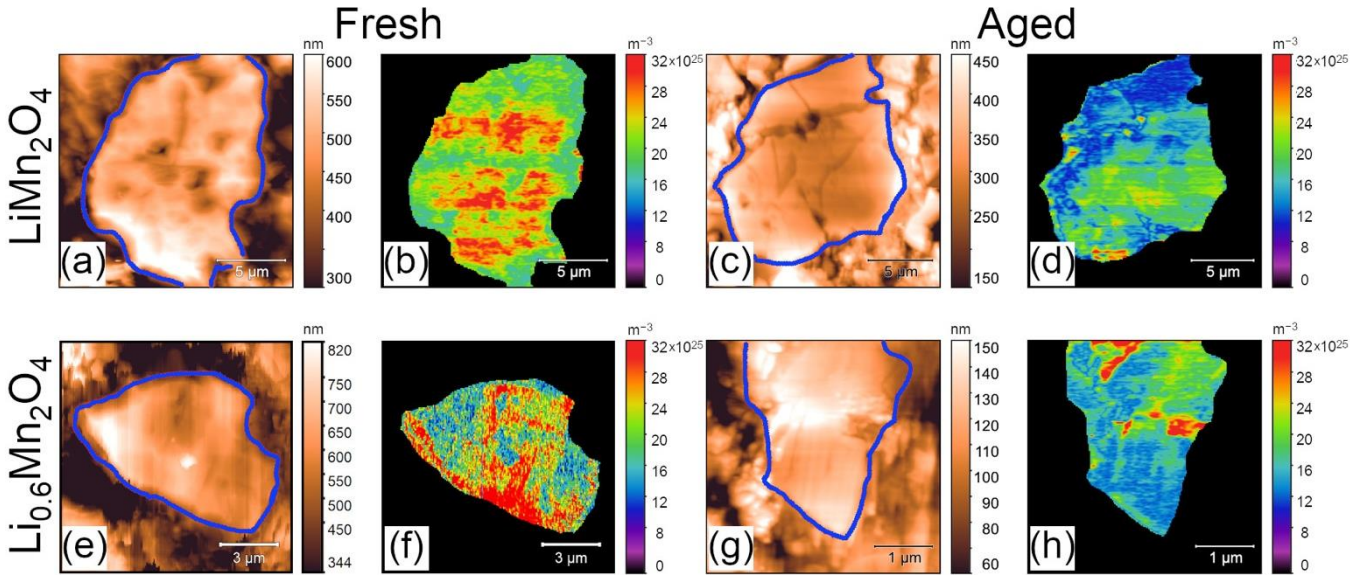

Figure 2. (**a**,**c**,**e**,**g**) Topography and (**b**,**d**,**f**,**h**) lithium ion concentration in (**a**–**d**) lithiated and (**e**–**h**) delithiated particles from (**a**,**b**,**e**,**f**) fresh and (**c**,**d**,**g**,**h**) aged cathodes.

The average concentrations of lithium ions calculated from the histograms in lithiated and delithiated cathodes are close to those calculated from X-ray diffraction data (Figure 3 and Table 1). The variation in the average concentration in the cathodes with the same SOC and SOH did not exceed 20%, and the concentration distribution is similar for the particles of similar size. It should be noted here, that the fitting of the region of the aged cathodes without actual data points is due to the limit of strain detection (below 0.5 pm), which

corresponds to the concentration below ~8 × 10^{25} m^{-3} (Figure 3). The concentration of lithium ions decreases with cycling, which can be directly related to capacity fade (Figure 3). A difference in the average ion concentrations in lithiated and delithiated cathodes slightly increases with cycling, which is a consequence of the significant histogram widening. An increase of the histogram width corresponds to a more heterogeneous distribution of lithium ions in aged cathodes (Figure 3), which develops an intuition about partial exclusion regions of the particles from the lithiation/delithiation process as a result of battery degradation.

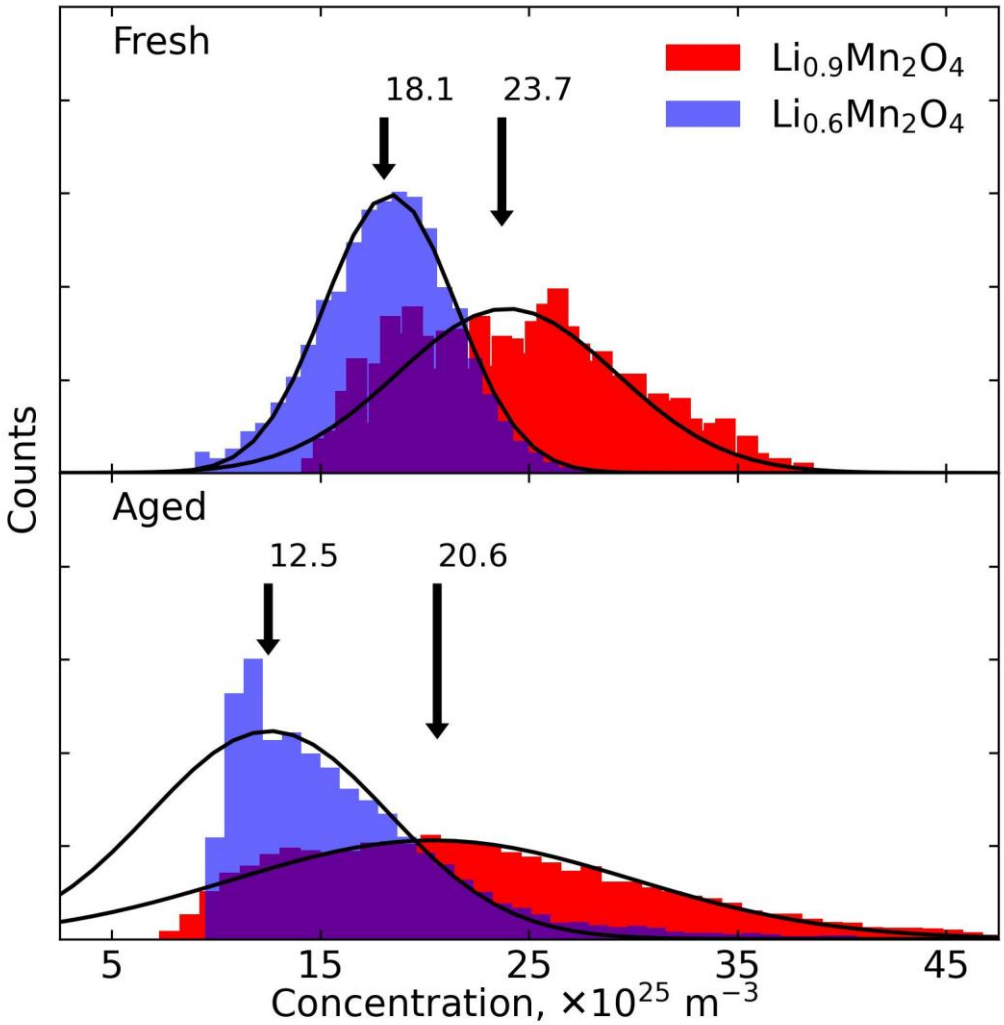

Figure 3. Histograms of lithium ion concentration in fresh and aged LMO cathodes extracted from ESM images. Black arrows indicate average concentrations.

An increase in the lithium ion concentration in the center of particles is observed for both fresh and aged lithiated cathodes (Figure 2b,d), which indicates more intense lithiation/delithiation kinetics near the edges of the particles, while the core of the particle delithiates slower. In delithiated cathodes, isolated regions with higher lithium concentrations mainly appear near the edges and cracks in particles (Figure 2f,h). An increase in lithium ion concentration near the particle edge in delithiated cathodes can be explained by the formation of the potential barriers along the particle/electrolyte interface, preventing lithium extraction [40]. This can be indirectly confirmed by the inspection of the local diffusion coefficients, verifying the existence of the <10 nm thick layer in this region (Figure 4f, inset). The existence of a thin inactive layer with lower diffusion coefficients is more apparent for the fresh cathodes compared to the aged ones, where ion concentration is distributed

more randomly across the particle. The confined areas with a higher ion concentration (comparable to the one in the lithiated cathodes) in the particles of the delithiated aged cathodes indicate isolated regions of the cathode that are excluded from the subsequent lithiation/delithiation process.

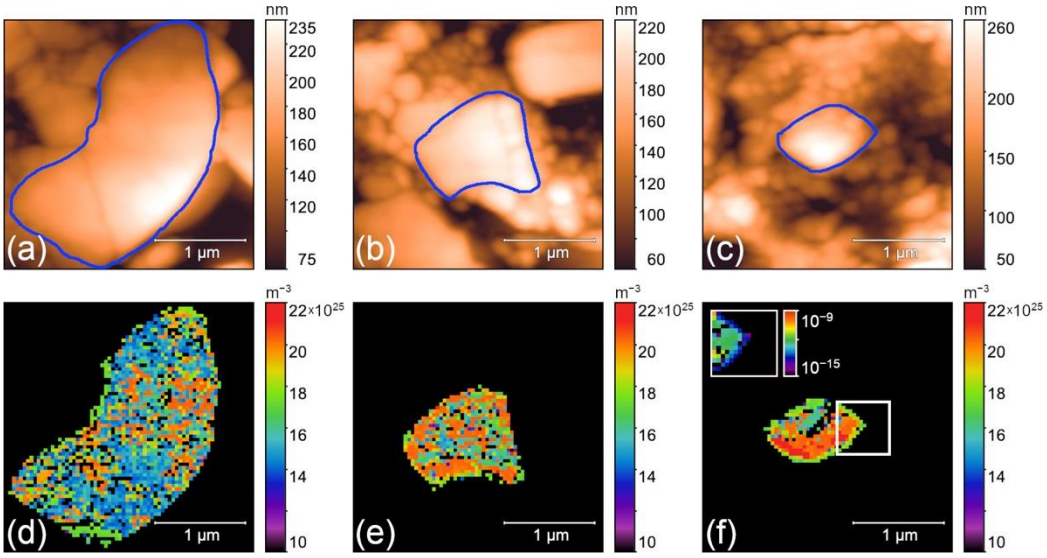

Figure 4. (**a**–**c**) Topography and (**d**–**f**) lithium ion concentration in the fresh $Li_{0.6}Mn_2O_4$. At (**f**) inset: variation in diffusion coefficient near the particle border.

The kinetics of lithiation also depends on the particle size, which has been revealed by the analysis of fresh delithiated cathodes (Figure 4). Small (less than 1 μm) particles typically reveal the apparent formation of the lithiated core and delithiated shell (Figure 4e,f). At the same time, in bigger particles, lithium ions become more homogeneously distributed. Nevertheless, formation of the confined lithiated regions inside individual large particles and, as discussed above, lithium ion segregation near the core of the particle was observed (Figure 4e,f).

4. Discussion

Currently, two basic models of lithiation kinetics are widely accepted: (1) the radial core–shell model (Figure 5a–c) and (2) the mosaic model (Figure 5d–f). In the frame of the radial core–shell model, the delithiation starts from the edges of the cathode particles due to the electromigration of the lithium ions into the electrolyte [41]. Lithium ions from the center of the particle (core) must diffuse through the thick delithiated layer (shell) in order to be extracted from the particle (Figure 5a,b). The process of delithiation is current-limited, and the value of the current is determined by the surface area of the lithiated phase in the particle. The process becomes diffusion-limited when the electromigration rate of lithium ions transported across the interface is no longer able to sustain the current. The gradual decrease in the maximal achievable current density decelerates and finally stops the extraction of the lithium ions from the particle core, which results in the formation of an inactive lithiated core in the center of the particle after completing the battery charge (Figure 5b). Another possible origin of the lithiated "core" formation is in the reduction in the electronic current flow in the delithiated phase [42,43], which also limits the maximal ionic current for keeping charge neutrality inside the particle [43]. The next lithiation cycle during battery discharge starts as well from the edges of the particle, but the lithiation front does not reach the residual lithiated core and it remains enclosed by the thin delithiated layer (Figure 5c). In the next cycles, this area becomes excluded from the lithiation/delithiation paths, which leads to overall capacitance reduction. The origin of the incomplete re-lithiation of the

batteries is not apparent and may have a random character or be a result of the stress relief between the lithiated and delithiated part of the particle, discussed later in the manuscript.

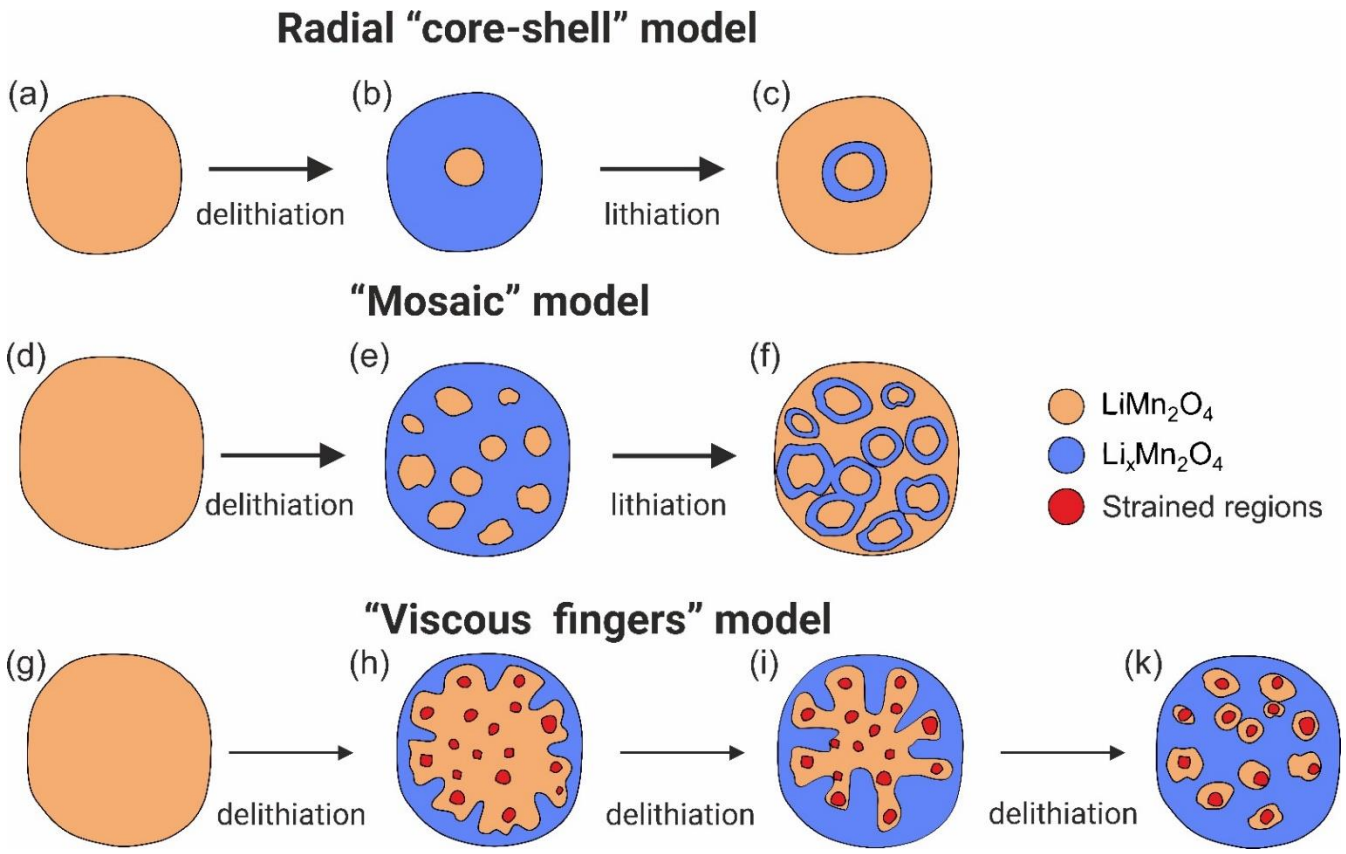

Figure 5. Kinetic models of lithiation/delithiation: (**a**–**c**) radial "core–shell" model [41,43], (**d**–**f**) "mosaic" model [43], (**g**–**k**) "viscous fingers" model.

An alternative model, the so-called "mosaic model", was proposed by Andersen and Thomas [44]. According to this model, delithiation starts from several sites inside the particle (Figure 5d), which leads to the formation of the spatially separated regions of residual inactive lithiated phase (Figure 5e), a "mosaic", excluded from the subsequent lithiation/delithiation cycles, similarly to what happens in the radial model (Figure 5f). A principal drawback of the mosaic model is the absence of any physical argument for starting the delithiation from several centers inside the particles, while the gradient of the lithium ion concentration is maximal near the electrolyte–particle interface.

Our results demonstrate that the radial model adequately describes lithiation kinetics in relatively small particles (less than 1 μm), while when several lithiated areas appear in large particles, the lithiation kinetics better corresponds to the mosaic model. At the same time, lithium-rich regions were forming not only at the particle edges in delithiated cathodes but also in the material bulk. We propose an alternative model for the description of lithium ion kinetics in large micrometer-scale particles in the LMO-based cathodes (Figure 5g–k). Significant heterogeneity is inherent in commercially available cathodes, which is discussed in Section 1. Heterogeneity is supposed to be caused by a disturbance of the electrical contacts [16] or stress relief in the particles caused by the "over-lithiation" in the local overpotentials, twinned boundaries [6], or defects. The contact disruption can be suggested to be responsible for the formation of the non-homogeneous lithiation at the particles' edges. Our earlier studies of the cathodes by confocal Raman microscopy confirmed the appearance of the regions of the inactive Mn_3O_4 phase in fresh delithiated cathodes [12]. The formation of the surface inactive layer revealed by ESM manifests the formation of electrode electrolyte interphase (EEI), which can influence the electrical contact

between the particles and the electrolyte. The passive layer at the particle surface hampers lithium extraction during lithiation and stimulates the formation of the lithium-rich regions near the particle edges (Figure 2f,h).

On the other hand, our measurements revealed many lithiated areas inside delithiated particles. Measurements by the confocal Raman spectroscopy also show areas with the widening of the A_{1g} band, which is supposed to reflect the inhomogeneity of the stress distribution inside the particles [12,14] (see Appendix A). The existence of the stress is confirmed by the massive cracking of the particles during cycling (Figure 2a,c,e,g). Thus, the lithiation occurs not only in the presence of the lithium ion concentration gradient in the vicinity of the particle edges, but also in the presence of the local gradients of lithium ion concentration inside the bulk, caused by the inhomogeneous distribution of the elastic fields. Initial instability of the reaction front from the inhomogeneity of the contacts and local heterogeneity of the particles themselves—residual mechanical stresses, twinned boundaries, and defects—can trigger the further non-uniform motion of the reaction front. Local acceleration and deceleration of the lithium extraction rate inside the particle evoke a distortion of the moving $Li_xMn_2O_4/LiMn_2O_4$ chemical reaction front (Figure 5h,i). Such a behavior can be described in the frame of the classical model of "viscous fingers" originating from the studies of fluid dynamics [45] and other critical phenomena at the liquid–liquid and liquid–solid interfaces with non-linear dynamics. Nevertheless, there are examples of critical phenomena with non-linear dynamics on the "solid–solid" interface, where a break of the phase boundary shape stability is observed: formation of dendrites in all-solid lithium batteries [46], glass crystallization [47], formation of ferroelectric and ferromagnetic domains [48–50] with irregular-shape domain walls. Among the mentioned systems, the lithiation of the materials is the most similar to ferroelectric domain growth, where viscosity and irregularity of the domain walls are consequences of the charge dynamics and electrostatic interaction [51,52]. One more fact to confirm the "viscous finger" model of lithiation/delithiation is recently published in situ TEM measurements of the $LiMn_2O_4$ lithiation to $Li_2Mn_2O_4$ state, which shows the irregular shape of the lithiation front and even the formation of individual fingers [6]. The mechanical compensation of the elastic fields resulted to the twinning in the active particles, which in turn created a diversity of the diffusion coefficient [6]. The velocity of the lithiation front motion in this research was closed both to a characteristic velocity of the viscoelastic solids [53] and domain wall dynamics in ferroelastics–ferroelectrics [54].

In the "viscous finger" model, the phase boundary (interface between lithiated and delithiated LMO) propagates spatially nonuniformly with different local rates, which leads to the loss of its stability (Figure 5h,i) and the formation of regions with residual lithiated phase (Figure 5k). The resulting distribution of the lithium ion concentration originating from the discussed model is in full accordance with the mosaic model but has a solid physical basis. The transformation of the lithiation kinetics from the "viscous fingers" model to the radial "core–shell" model can be explained by the reduction in the compositional and structural heterogeneity in the small-size particles. Certainly, suggested phenomenological model is fully qualitative and needs more detailed study, e.g., with in situ experiments and modeling, which is highly desirable but out of the scope of the current report.

A capacitance fade caused by the formation of the isolated regions in the particles during lithiation–delithiation cycle can be overcome by reduction of the particles' size. The reduced particle size would help to suppress the formation of multiple cores—residual lithiated regions. An additional surface coating of the particles protecting from manganese dissolution or doping by ions, stabilizing the structure of LMO, can be used to improve electrical contact [55]. This would be essential for reducing the ion segregation near the surface and the homogenization of the lithiation process. From this point, the implementation of the nanostructured cathodes (nanorods, nanoparticles, etc.) appears attractive for the further development of the material.

5. Conclusions

Lithiation kinetics were studied in commercial LMO-based battery materials using electrochemical strain microscopy. The distribution of the lithium ions in the active particles was visualized depending on the cathode "state of charge", "state of health", and an average grain size. The relatively small particles (less than 1 μm) were found to be delithiated following well-known radial "core–shell" model, while larger-scale particles possess a number of lithiation sites and some of them in the particle volume. The formation of the "mosaic" distribution of the lithiated area followed by the respective stress relief was described on the basis of the "viscous fingers" model invoked for the lithiation kinetics of LMO cathodes, which expands our understanding of the intercalation process and enables further control of the capacity fade in LMO.

Author Contributions: Investigation, D.A., B.S.; methodology, D.A., B.S.; formal analysis, D.A., B.S.; writing—original draft preparation, D.A., B.S., A.K. All authors have read and agreed to the published version of the manuscript.

Funding: The research funding from the Ministry of Science and Higher Education of the Russian Federation (Ural Federal University Program of Development within the Priority-2030 Program) is gratefully acknowledged.

Institutional Review Board Statement: Not applicable.

Informed Consent Statement: Not applicable.

Data Availability Statement: The initial data presented in this study are available on request from the corresponding author. The data are not publicly available due to large data size.

Acknowledgments: The equipment of the Ural Center for Shared Use "Modern nanotechnology" of Ural Federal University (Reg. # 2968), which is supported by the Ministry of Science and Higher Education RF (Project # 075-15-2021-677), was used.

Conflicts of Interest: The authors declare no conflict of interest. The founding sponsors had no role in the design of the study; in the collection, analyses, or interpretation of data; in the writing of the manuscript, and in the decision to publish the results.

Appendix A. Correlative ESM and Confocal Raman Microscopy (CRM) Measurements

The details of ESM measurements can be found in Section 2. ESM and CRM measurements were performed separately on the same particle detected by optical microscopy. CRM measurements were performed using the confocal Raman microscope (Alpha 300 AR, WiTec GmbH, Ulm, Germany). A 488 nm laser was used for the measurements, which was focused through a ×100 objective. The reflected light was analyzed using 1800 grids/mm grating. Scanning was performed using the piezoelectrically driven stage. Raman spectra were accumulated over 25 s. All collected spectra were normalized by the area and fitted using the superposition of Lorentzian. The distribution of full width at half maximum of the A_{1g} Raman peak inside the particle was plotted in the pseudo-color scale (Figure A1c). More details about CRM measurements and analysis can be found elsewhere [12].

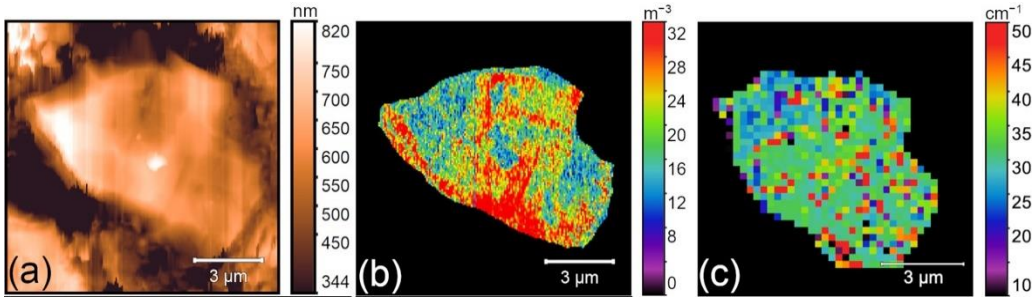

Figure A1. Correlative ESM and CRM measurements performed on the active particle of fresh $Li_{0.6}Mn_2O_4$. (**a**) Topography, (**b**) lithium ion concentration, and (**c**) FWHM of A1g Raman peak.

References

1. Ohzuku, T. Electrochemistry of manganese dioxide in lithium nonaqueous cell. *J. Electrochem. Soc.* **1990**, *137*, 769–775. [CrossRef]
2. Julien, C.; Mauger, A.; Vijh, A.; Zaghib, K. *Lithium Batteries*; Springer: Cham, Switzerland, 2016.
3. Zhan, C.; Wu, T.; Lu, J.; Amine, K. Dissolution, migration, and deposition of transition metal ions in Li-Ion batteries exemplified by Mn-based cathodes—A critical review. *Energy Environ. Sci.* **2018**, *11*, 243–257. [CrossRef]
4. Luo, F.; Wei, C.; Zhang, C.; Gao, H.; Niu, J.; Ma, W.; Peng, Z.; Bai, Y.; Zhang, Z. Operando X-ray diffraction analysis of the degradation mechanisms of a spinel $LiMn_2O_4$ cathode in different voltage windows. *J. Energy Chem.* **2020**, *44*, 138–146. [CrossRef]
5. Yang, P.; Bi, Z.; Shang, Y.; Chen, K.; Liang, Y.; Li, X.; Shang, G. Bimodal AFM-Based nanocharacterization of cycling-induced topographic and mechanical evolutions of $LiMn_2O_4$ cathode films. *Langmuir* **2021**, *37*, 6406–6413. [CrossRef] [PubMed]
6. Erichsen, T.; Pfeiffer, B.; Roddatis, V.; Volkert, C.A. Tracking the diffusion-controlled lithiation reaction of $LiMn_2O_4$ by in situ TEM. *ACS Appl. Energy Mater.* **2020**, *3*, 5405–5414. [CrossRef]
7. Wohlfahrt-Mehrens, M.; Vogler, C.; Garche, J. Aging mechanisms of lithium cathode materials. *J. Power Sources* **2004**, *127*, 58–64. [CrossRef]
8. Hausbrand, R.; Cherkashinin, G.; Ehrenberg, H.; Gröting, M.; Albe, K.; Hess, C.; Jaegermann, W. Fundamental degradation mechanisms of layered oxide Li-ion battery cathode materials: Methodology, insights and novel approaches. *Mater Sci. Eng. B* **2015**, *192*, 3–25. [CrossRef]
9. Gummow, R.J.; de Kock, A.; Thackeray, M.M. Improved capacity retention in rechargeable 4 V lithium/lithium-manganese Oxide (Spinel) Cells. *Solid State Ion.* **1994**, *69*, 59–67. [CrossRef]
10. Xia, Y.; Zhou, Y.; Yoshio, M. Capacity fading on cycling of 4 V $Li/LiMn_2O_4$ cells. *J. Electrochem. Soc.* **1997**, *144*, 2593–2600. [CrossRef]
11. Tang, D.; Sun, Y.; Yang, Z.; Ben, L.; Gu, L.; Huang, X. Surface structure evolution of $LiMn_2O_4$ cathode material upon charge/discharge. *Chem. Mater.* **2014**, *26*, 3535–3543. [CrossRef]
12. Slautin, B.; Alikin, D.; Rosato, D.; Pelegov, D.; Shur, V.; Kholkin, A. Local study of lithiation and degradation paths in $LiMn_2O_4$ battery cathodes: Confocal Raman microscopy approach. *Batteries* **2018**, *4*, 21. [CrossRef]
13. Jang, D.H.; Shin, Y.J.; Oh, S.M. Dissolution of spinel oxides and capacity losses in 4 V Li / $Li_xMn_2O_4$ cells. *J. Electrochem. Soc.* **1996**, *143*, 2204–2211. [CrossRef]
14. Julien, C.M.; Massot, M. Lattice vibrations of materials for lithium rechargeable batteries I. Lithium manganese oxide spinel. *Mater Sci. Eng. B* **2003**, *97*, 217–230. [CrossRef]
15. Ramana, C.V.; Massot, M.; Julien, C.M. XPS and Raman spectroscopic characterization of $LiMn_2O_4$ spinels. *Surf. Interface Anal.* **2005**, *37*, 412–416. [CrossRef]
16. Greeley, J.; Warburton, R.E.; Castro, F.C.; Deshpande, S.; Madsen, K.E.; Bassett, K.L.; dos Reis, R.; Gewirth, A.A.; Dravid, V.P. Oriented $LiMn_2O_4$ particle fracture from delithiation-driven surface stress. *ACS Appl. Mater. Interfaces* **2020**, *12*, 49182–49191.
17. Thackeray, M.M.; Johnson, P.J.; de Picciotto, L.A.; Bruce, P.G.; Goodenough, J.B. Electrochemical extraction of lithium from $LiMn_2O_4$. *Mater. Res. Bull.* **1984**, *19*, 179–187. [CrossRef]
18. Thackeray, M.M.; Shao-Horn, Y.; Kahaian, A.J.; Kepler, K.D.; Skinner, E.; Vaughey, J.T.; Hackney, S.A. Structural fatigue in spinel electrodes in high voltage (4 V) $Li/Li_xMn_2O_4$ cells. *Electrochem. Solid State Lett.* **1998**, *1*, 7–9. [CrossRef]
19. Liu, Z.; Han, K.; Chen-Wiegart, Y.K.; Wang, J.; Kung, H.H.; Wang, J.; Barnett, S.A.; Faber, K.T. X-Ray nanotomography analysis of the microstructural evolution of $LiMn_2O_4$ electrodes. *J. Power Sources* **2017**, *360*, 460–469. [CrossRef]
20. Chen, G.; Song, X.; Richardson, T.J. Electron microscopy study of the $LiFePO_4$ to $FePO_4$ phase transition. *Electrochem. Solid State Lett.* **2006**, *9*, A295–A298. [CrossRef]
21. Lee, S.; Oshima, Y.; Hosono, E.; Zhou, H.; Kim, K.; Chang, H.M.; Kanno, R.; Takayanagi, K. In situ TEM observation of local phase transformation in a rechargeable $LiMn_2O_4$ nanowire battery. *J. Phys. Chem. C* **2013**, *117*, 24236–24241. [CrossRef]
22. Okubo, M.; Mizuno, Y.; Yamada, H.; Kim, J.; Hosono, E.; Zhou, H.; Kudo, T.; Honma, I. Fast Li-ion insertion into nanosized $LiMn_2O_4$ without domain boundaries. *ACS Nano* **2010**, *4*, 741–752. [CrossRef] [PubMed]
23. Wolfman, M.; Khawaja, S.; Cabana, J. Mapping and metastability of heterogeneity in $LiMn_2O_4$ battery electrodes with high energy density. *J. Electrochem. Soc.* **2020**, *167*, 020526. [CrossRef]
24. Wang, F.; Yang, K.; Ge, M.; Wang, J.; Wang, J.; Xiao, X.; Lee, W.-K.; Li, L.; Tang, M. Reaction heterogeneity in $LiFePO_4$ agglomerates and the role of intercalation-induced stress. *ACS Energy Lett.* **2022**, *7*, 1648–1656. [CrossRef]
25. Welland, M.J.; Karpeyev, D.; O'Connor, D.T.; Heinonen, O. Miscibility gap closure, interface morphology, and phase microstructure of 3D Li_xFePO_4 nanoparticles from surface wetting and coherency strain. *ACS Nano* **2015**, *9*, 9757–9771. [CrossRef]
26. Lou, S.; Liu, Q.; Zhang, F.; Liu, Q.; Yu, Z.; Mu, T.; Zhao, Y.; Borovilas, J.; Chen, Y.; Ge, M.; et al. Insights into interfacial effect and local lithium-ion transport in polycrystalline cathodes of solid-state batteries. *Nat. Commun.* **2020**, *11*, 5700. [CrossRef]
27. Yu, Y.S.; Kim, C.; Shapiro, D.A.; Farmand, M.; Qian, D.; Tyliszczak, T.; Kilcoyne, A.L.D.; Celestre, R.; Marchesini, S.; Joseph, J.; et al. Dependence on crystal size of the nanoscale chemical phase distribution and fracture in Li_xFePO_4. *Nano Lett.* **2015**, *15*, 4282–4288. [CrossRef]

28. Schön, N.; Schierholz, R.; Jesse, S.; Yu, S.; Eichel, R.A.; Balke, N.; Hausen, F. Signal origin of electrochemical strain microscopy and link to local chemical distribution in solid state electrolytes. *Small Methods* **2021**, *5*, 2001279. [CrossRef]
29. Li, Y.; Weker, J.N.; Gent, W.E.; Mueller, D.N.; Lim, J.; Cogswell, D.A.; Tyliszczak, T.; Chueh, W.C. Dichotomy in the lithiation pathway of ellipsoidal and platelet LiFePO4 particles revealed through nanoscale operando state-of-charge imaging. *Adv. Funct. Mater.* **2015**, *25*, 3677–3687. [CrossRef]
30. Yu, Y.S.; Farmand, M.; Kim, C.; Liu, Y.; Grey, C.P.; Strobridge, F.C.; Tyliszczak, T.; Celestre, R.; Denes, P.; Joseph, J.; et al. Three-dimensional localization of nanoscale battery reactions using soft X-Ray tomography. *Nat. Commun.* **2018**, *9*, 921. [CrossRef]
31. Balke, N.; Jesse, S.; Kim, Y.; Adamczyk, L.; Ivanov, I.N.; Dudney, N.J.; Kalinin, S.V. Decoupling electrochemical reaction and diffusion processes in ionically-conductive solids on the nanometer scale. *ACS Nano* **2010**, *4*, 7349–7357. [CrossRef]
32. Alikin, D.O.; Romanyuk, K.N.; Slautin, B.N.; Rosato, D.; Shur, V.Y.; Kholkin, A.L. Quantitative characterization of the ionic mobility and concentration in li-battery cathodes via low frequency electrochemical strain microscopy. *Nanoscale* **2018**, *10*, 2503–2511. [CrossRef] [PubMed]
33. Alikin, D.O.; Ievlev, A.V.; Luchkin, S.Y.; Turygin, A.P.; Shur, V.Y.; Kalinin, S.V.; Kholkin, A.L. Characterization of $LiMn_2O_4$ cathodes by electrochemical strain microscopy. *Appl. Phys. Lett.* **2016**, *108*, 113106. [CrossRef]
34. Romanyuk, K.N.; Alikin, D.O.; Slautin, B.N.; Tselev, A.; Shur, V.Y.; Kholkin, A.L. Local electronic transport across probe/ionic conductor interface in Scanning Probe Microscopy. *Ultramicroscopy* **2021**, *220*, 113147. [CrossRef] [PubMed]
35. Alikin, D.; Slautin, B.; Abramov, A.; Rosato, D.; Shur, V.; Tselev, A.; Kholkin, A. correlative confocal raman and scanning probe microscopy in the ionically active particles of $LiMn_2O_4$ cathodes. *Materials* **2019**, *12*, 1416. [CrossRef] [PubMed]
36. Luchkin, S.Y.; Amanieu, H.Y.; Rosato, D.; Kholkin, A.L. Li distribution in graphite anodes: A Kelvin Probe Force Microscopy approach. *J. Power Sources* **2014**, *268*, 887–894. [CrossRef]
37. Kuriyama, K.; Onoue, A.; Yuasa, Y.; Kushida, K. Atomic force microscopy study of surface morphology change in spinel $LiMn_2O_4$: Possibility of direct observation of Jahn-Teller instability. *Surf. Sci.* **2007**, *601*, 2256–2259. [CrossRef]
38. Arruda, T.M.; Kumar, A.; Kalinin, S.V.; Jesse, S. The partially reversible formation of Li-metal particles on a solid li electrolyte: Applications toward nanobatteries. *Nanotechnology* **2012**, *23*, 325402. [CrossRef]
39. Balke, N.; Jesse, S.; Yu, P.; Carmichael, B.; Kalinin, S.V.; Tselev, A. Quantification of surface displacements and electromechanical phenomena via dynamic atomic force microscopy. *Nanotechnology* **2016**, *27*, 425707. [CrossRef]
40. McGrogan, F.P.; Raja, S.N.; Chiang, Y.-M.; van Vliet, K.J. Electrochemomechanical fatigue: Decoupling mechanisms of fracture-induced performance degradation in $Li_xMn_2O_4$. *J. Electrochem. Soc.* **2018**, *165*, A2458–A2466. [CrossRef]
41. Padhi, A.K.; Nanjundaswamy, K.S.; Goodenough, J.B. Phospho-olivines as positive-electrode materials for rechargeable lithium batteries. *J. Electrochem. Soc.* **1997**, *144*, 1188–1194. [CrossRef]
42. Yamamura, S.; Koshika, H.; Nishizawa, M.; Matsue, T.; Uchida, I. In situ conductivity measurements of $LiMn_2O_4$ thin films during lithium insertion/extraction by using interdigitated microarray electrodes. *J. Solid State Electrochem.* **1998**, *2*, 211–215. [CrossRef]
43. Luchkin, S.Y.; Kirsanova, M.A.; Aksyonov, D.A.; Lipovskikh, S.A.; Nikitina, V.A.; Abakumov, A.M.; Stevenson, K.J. Cycling-driven electrochemical activation of Li-rich NMC positive electrodes for li-ion batteries. *ACS Appl. Energy Mater.* **2022**, *5*, 7758–7769. [CrossRef]
44. Andersson, A.S.; Thomas, J.O. The source of first-cycle capacity loss in LiFePO4. *J. Power Sources* **2001**, *97*, 498–502. [CrossRef]
45. Zimmerman, W.B.; Homsy, G.M. Nonlinear viscous fingering in miscible displacement with anisotropic dispersion. *Phys. Fluids* **1991**, *3*, 1859–1872. [CrossRef]
46. Love, C.T.; Baturina, O.A.; Swider-Lyons, K.E. Observation of lithium dendrites at ambient temperature and below. *ECS Electrochem. Lett.* **2015**, *4*, A24–A27. [CrossRef]
47. Allix, M.; Cormier, L. Crystallization and glass-ceramics. In *Book Springer Handbook of Glass*, 1st ed.; Musgraves, J.D., Hu, J., Calvez, L., Eds.; Springer: Cham, Switzerland, 2019; pp. 113–167.
48. Sato, H.; Enobio, E.C.I.; Yamanouchi, M.; Ikeda, S.; Fukami, S.; Kanai, S.; Matsukura, F.; Ohno, H. Properties of magnetic tunnel junctions with a MgO/CoFeB/Ta/CoFeB/MgO recording structure down to junction diameter of 11 nm. *Appl. Phys. Lett.* **2014**, *105*, 062403. [CrossRef]
49. Grassi, M.P.; Kolton, A.B.; Jeudy, V.; Mougin, A.; Bustingorry, S.; Curiale, J. Intermittent collective dynamics of domain walls in the creep regime. *Phys. Rev. B* **2018**, *98*, 224201. [CrossRef]
50. Diáz Pardo, R.; Moisan, N.; Albornoz, L.J.; Lemaître, A.; Curiale, J.; Jeudy, V. Common universal behavior of magnetic domain walls driven by spin-polarized electrical current and magnetic field. *Phys. Rev. B* **2019**, *100*, 184420. [CrossRef]
51. Turygin, A.P.; Alikin, D.O.; Kosobokov, M.S.; Ievlev, A.V.; Shur, V.Y. Self-organized formation of quasi-regular ferroelectric nanodomain structure on the nonpolar cuts by grounded SPM tip. *ACS Appl. Mater. Interfaces* **2018**, *10*, 36211–36217. [CrossRef]
52. Tikhonov, Y.; Maguire, J.R.; McCluskey, C.J.; McConville, J.P.V.; Kumar, A.; Lu, H.; Meier, D.; Razumnaya, A.; Gregg, J.M.; Gruverman, A.; et al. Polarization topology at the nominally charged domain walls in uniaxial ferroelectrics. *Adv. Mater.* **2022**, 2203028. Available online: https://onlinelibrary.wiley.com/doi/10.1002/adma.202203028 (accessed on 1 November 2022). [CrossRef]
53. Amann, C.P.; Siebenbürger, M.; Krüger, M.; Weysser, F.; Ballauff, M.; Fuchs, M. Overshoots in stress-strain curves: Colloid experiments and schematic mode coupling theory. *J. Rheol.* **2013**, *57*, 149–175. [CrossRef]

54. Scott, J.F.; Kumar, A. Faceting oscillations in nano-ferroelectrics. *Appl. Phys. Lett.* **2014**, *105*, 052902. [CrossRef]
55. Radzi, Z.I.; Arifin, K.H.; Kufian, M.Z.; Balakrishnan, V.; Raihan, S.R.S.; Rahim, N.A.; Subramaniam, R. Review of spinel $LiMn_2O_4$ cathode materials under high cut-off voltage in lithium-ion batteries: Challenges and strategies. *J. Electroanal. Chem.* **2020**, *920*, 116623. [CrossRef]